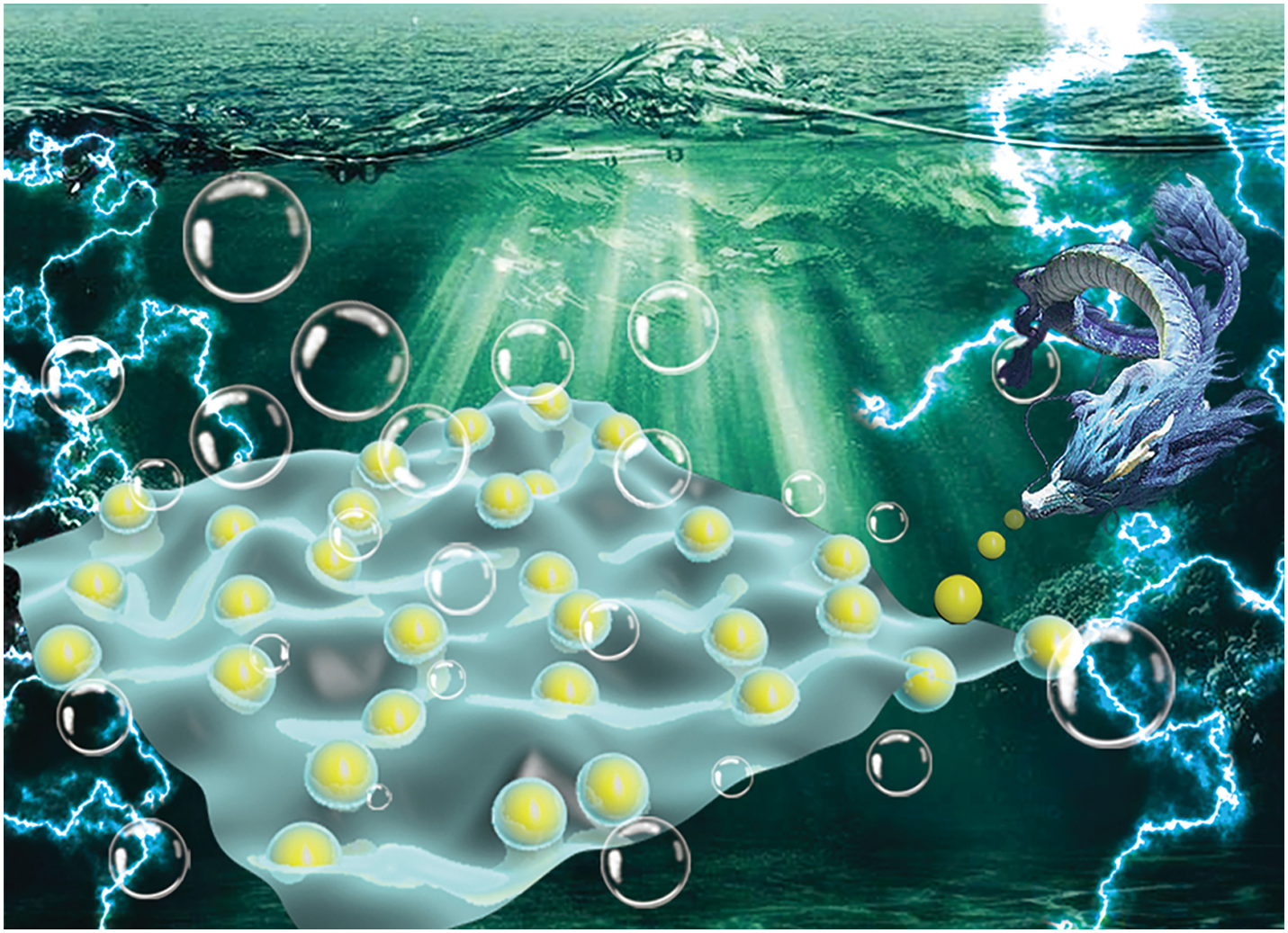

Showcasing research from Professor Dong-Sheng Li's laboratory, College of Materials and Chemical Engineering, China Three Gorges University, Yichang, China.

An amorphous NiS_x film as a robust cocatalyst for boosting photocatalytic hydrogen generation over ultrafine ZnCdS nanoparticles

Optimization of cocatalysts is promising and of great significance for greatly boosting photocatalytic activity as well as outstanding stability. An effective route was proposed to combine amorphous NiS_x films as a cocatalyst with embedded ultrafine ZnCdS nanoparticles *via* a photochemical deposition method. Amorphous NiS_x films can serve as electron collectors and conveyors as well as massive reduction active sites for H_2 production. The excellent photocatalytic H_2 generation of NiS_x/ZnCdS compositions is ascribed to the synergetic effects of the adequate interface contact and the efficient spatial separation of the charges.

As featured in:

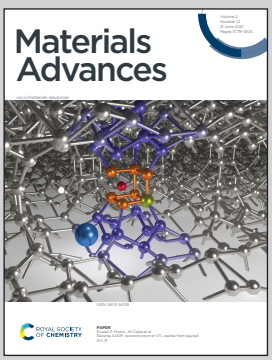

See Dongfang Hou, Dong-sheng Li *et al.*, *Mater. Adv.*, 2021, **2**, 3881.

ROYAL SOCIETY OF CHEMISTRY

rsc.li/materials-advances

Registered charity number: 207890

Materials Advances

ROYAL SOCIETY OF CHEMISTRY

PAPER

View Article Online
View Journal | View Issue

Cite this: *Mater. Adv.*, 2021, 2, 3881

An amorphous NiS_x film as a robust cocatalyst for boosting photocatalytic hydrogen generation over ultrafine ZnCdS nanoparticles†

Shenglong Gan, Min Deng, Dongfang Hou,* Lei Huang, Xiu-qing Qiao and Dong-sheng Li *

Received 27th January 2021,
Accepted 13th April 2021

DOI: 10.1039/d1ma00067e

rsc.li/materials-advances

Optimization of cocatalysts is promising and of great significance in enhancing photocatalytic H_2 generation from the perspective of understanding the charge separation, surface reaction kinetics, and distribution of active sites. Herein, we synthesize a class of well-formed hybrid photocatalysts by coupling amorphous NiS_x films to ultrafine ZnCdS nanoparticles for greatly boosting the photocatalytic activity as well as the outstanding stability and repeatability. Under visible-light irradiation, the highest H_2 evolution rate of the as-synthesized NiS_x/ZnCdS photocatalyst achieved is 67.75 mmol g^{-1} h^{-1}, which is 28.8 times higher than that of Pt/ZnCdS. Further detailed characterization reveals that the amorphous NiS_x film as an excellent cocatalyst not only improves the spatial separation of the photoinduced carriers but also collects electrons and enlarges the reduction reaction space. This work could provoke interest in understanding the spatial charge migration in the cocatalyst system with an amorphous film structure, thus developing high-performance low-cost composite photocatalysts for H_2 production.

Introduction

Hydrogen energy will be considerable in prospective sustainable energy societies because it is clean, storable, and transportable.[1–3] Hydrogen production from water decomposition on photocatalysts is an efficient way to transform inexhaustible solar energy to hydrogen energy.[4,5] Nowadays, more and more endeavors are devoted to the development of highly active photocatalysts with low cost.[6–10] As we know, the photocatalytic performance of hydrogen production of the given photocatalyst is limited by some essential factors, such as light harvesting properties, charge separation and transportation at the active site and surface catalytic reduction reactions, and so on.[7,11–13] It is worth noting that cooperating with a cocatalyst is an effective route to be conducive to the balance of the above thermodynamic and kinetic processes and improvement of the photocatalytic activity. Thus, the optimization design of the cocatalyst has drawn wide attention in this field.[14,15]

To date, numerous efforts have been devoted to understand and explore different cocatalysts and their functional applications, such as some noble metals (Pt, Au and Pd).[16–19] To reduce the cost of photocatalytic H_2 production, some inexpensive noble-metal-free cocatalysts have been introduced in recent years.[11] Interestingly, it has been also revealed that the microstructure of the cocatalyst itself also plays an important role in high activity photocatalytic systems, such as the crystal structure, morphology, and crystallinity.[20–22] Generally amorphous structures with a high density of defective sites and dangling bonds receive more and more attention as photocatalysts and electrocatalysts.[23,24] However, only a few researchers focus on the amorphous cocatalysts for photocatalytic H_2 production.[25–27] These works indicated that the amorphous cocatalysts could remarkably promote charge transfer and provide more active sites for photocatalytic reactions.[26] For instance, Liu *et al.*[27] prepared amorphous NiO modified g-C_3N_4 for visible-light photocatalytic hydrogen evolution and demonstrated the improved migration and separation of photogenerated charge carriers. In addition, to increase the electron outlet points between photoactive materials and cocatalysts, various morphologies of cocatalysts and surface integrated forms of them have also been studied widely.[28] It is remarkable that cocatalysts in the form of films can enlarge the contact area and alleviate external energy loss during long-distance transportation between the separated photo-absorbers and reactive site centers.[29] The exploration of efficient amorphous photocatalysts therefore remains desirable yet challenging.

Up to now, great advances have been achieved to employ many electrocatalysts as cocatalysts in the photocatalytic H_2

College of Materials and Chemical Engineering, Hubei Provincial Collaborative Innovation Center for New Energy Microgrid, Key Laboratory of Inorganic Nonmetallic Crystalline and Energy Conversion Materials, China Three Gorges University, Yichang 443002, P. R. China. E-mail: dfhouok@126.com, lidongsheng1@126.com

† Electronic supplementary information (ESI) available: SEM images, XRD patterns, XPS spectra *etc.* See DOI: 10.1039/d1ma00067e

production.[30–32] Transition-metal sulfides such as nickel sulfides attracted many groups' attention as cost-effective and promising Pt-group metal candidates.[33,34] Most importantly, among all the non-precious metal species, nickel sulfides show a lower activation energy to form the Ni–H bond with the surface-adsorbed H_2O during proton reduction.[35–37] For example, Zhong *et al.* demonstrated that the amorphous nanocluster of NiS_{1+x} provides numerous active sites and accelerates the electron migration, which serves as an outstanding cocatalyst to boost the H_2 evolution rate of the NiS_{1+x}/TiO_2 photocatalyst.[25] Xue *et al.*[36] developed the novel NiS_2 quantum dot (QD) cocatalyst anchored on the surface of $Cd_{0.8}Zn_{0.2}S$/rGO nanosheet composites, which shows efficient photocatalytic hydrogen evolution. Obviously, these great studies have tuned the structure and morphology of cocatalysts so as to enhance the transmission efficiency of electrons. ZnCdS is one of the most broadly studied metal sulphide solid solutions because of its high H_2 evolution rate under visible light irradiation.[38] However, the conventional pure ZnCdS is still plagued by photocorrosion and poor spatial charge isolation. Reducing the particle size of the ZnCdS photocatalyst is one of the effective methods to enhance the charge-transfer rate which significantly diminishes the volume recombination of electron–hole pairs in the semiconductor material.[39] Ideally, if a strong alliance can be realized between the rationally designed NiS_x cocatalyst with an amorphous structure and the ultrafine ZnCdS particles, it is highly expectable that the photocatalytic H_2 generation activity may be further promoted. Unfortunately, related studies on the fabrication and properties of the system are still very rare.

Inspired by the above considerations, here, we present an effective route to combine the amorphous NiS_x films as the cocatalyst with ultrafine ZnCdS particles *via* a photochemical deposition method, which greatly boosts the photocatalytic hydrogen evolution performance. Impressively, the optimized NiS_x/ZnCdS photocatalyst reaches a remarkably promoted photocatalytic H_2-production rate of 67.75 mmol g^{-1} h^{-1} and the AQE of 10.24% (420 nm). Furthermore, its structural properties and the corresponding accelerated charge transfer dynamics were discussed based on many pieces of targeted characterization evidence. Amorphous NiS_x films can serve as electron collectors and conveyors as well as massive reduction active sites for H_2 production, which greatly contribute to the high photocatalytic performance. This work could be of interest in understanding the carrier separation form and increasingly turning to the design of highly efficient cocatalysts.

Experimental section

Materials

Cadmium acetate dihydrate ($Cd(CH_3COO)_2{\cdot}2H_2O$) was obtained from Tianjin Kemiou Chemical Reagent Co., Ltd. Zinc acetate dihydrate ($Zn(CH_3COO)_2{\cdot}2H_2O$) was obtained from Sinopharm Chemical Reagent Co., Ltd. Sodium sulfide nonahydrate ($Na_2S{\cdot}9H_2O$) was obtained from Aladdin Chemical Co., Ltd. Nickel acetate tetrahydrate ($Ni(CH_3COO)_2{\cdot}4H_2O$) was purchased from Shanghai Macklin Biochemical Co., Ltd. Thiourea (CH_4N_2S) and ethanol were purchased from Tianli Chemical Reagent Co., Ltd. All reagents were used without further purification.

Preparation of ultrafine ZnCdS nanoparticles

The ZnCdS nanoparticles were prepared by a simple hydrothermal method. In detail, 0.5 mmol $Cd(CH_3COO)_2{\cdot}2H_2O$ and 0.5 mmol $Zn(CH_3COO)_2{\cdot}2H_2O$ were dissolved in 20 mL of deionized water and stirred to ensure complete dissolution. 5 mL of Na_2S aqueous solution (0.3 mol L^{-1}) was added dropwise, followed by stirring for 2 h at room temperature. The suspension was transferred to a 50 mL inner Teflon-lined stainless steel autoclave and heated at 160 °C for 4 h. After cooling down to room temperature, the solid products were collected by centrifugation and washed three times with distilled water and ethanol, and then dried at 80 °C overnight. It is named ZCS. Using the same method, ZnS and CdS were synthesized without adding $Cd(CH_3COO)_2{\cdot}2H_2O$ and $Zn(CH_3COO)_2{\cdot}2H_2O$, respectively.

Preparation of NiS_x/ZnCdS

The NiS_x thin films loaded with ultrafine ZnCdS nanoparticle photocatalysts were prepared by a photochemical deposition method. In a typical procedure (see Fig. 1), 40 mg of ZnCdS was dispersed into the mixed solvent of 12 mL deionized water and 8 mL ethanol and then the mixture was placed in an ultrasonic bath to form a homogeneously dispersing suspension. Then certain amounts of $Ni(CH_3COO)_2{\cdot}4H_2O$ (0.025 mmol, 0.05 mmol, and 0.1 mmol) and CH_4N_2S (0.25 mmol, 0.5 mmol, and 1 mmol)

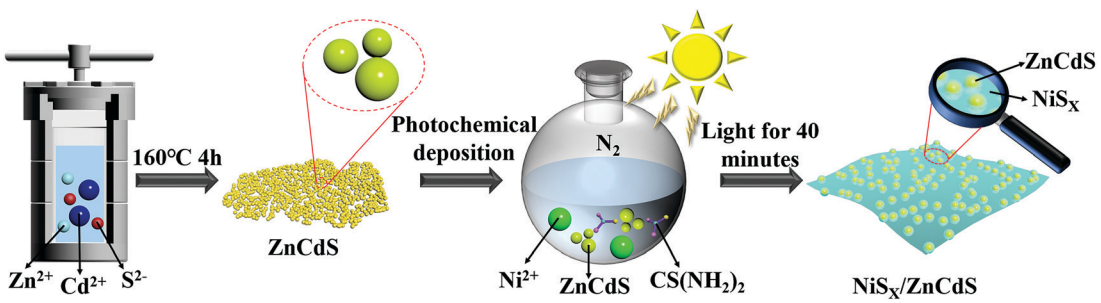

Fig. 1 Schematic representation of the synthesis of the NiS_x films/ultrafine ZCS nanoparticles.

were added rapidly under ultrasound. Subsequently, the homogeneous suspension was purged with nitrogen for 30 min to remove air. And the above treated solution was irradiated with a 300 W xenon lamp for 40 min to deposit a nickel sulfide film. Finally, the dark green products were collected by centrifugation and washing with water and alcohol three times, respectively, and dried in an 80 °C vacuum oven. The acquired samples were denoted as ZCS-NS1, ZCS-NS2, and ZCS-NS3, representing that the concentrations of nickel source were 0.025 mmol, 0.5 mmol and 0.1 mmol, respectively. Specifically, to learn more about the amorphous film, the sample with excess NiS_x film, labeled as ZCS-NSE, was obtained *via* increasing the amount of raw materials (1 mmol $Ni(CH_3COO)_2{\cdot}4H_2O$,and 10 mmol CH_4N_2S). In the same way, when ZnS and CdS were used instead of ZnCdS, and adding $Ni(CH_3COO)_2{\cdot}4H_2O$ and CH_4N_2S in an amount of 0.05 mmol and 0.5 mmol, respectively, we obtained the other two composite catalysts named ZS-NS and CS-NS.

Characterization

The crystal structure of the sample was analyzed using a Japanese Rigaku Ultima IV X-ray powder diffractometer (XRD, Cu-Kα) at 40 kV and 40 mA. The scanning range of the 2θ angle is 5°–80°. The morphology and microstructure of the samples were measured using a scanning electron microscope (SEM, JEOL JSM 7500F) and a transmission electron microscope (TEM, Tecnai G2 F20 S TWIN) equipped with an energy dispersive spectrometer (EDS). The surface chemical valence state was analyzed by X-ray photoelectron spectroscopy (XPS, Al-Kα) on an ESCALAB 250 X-ray photoelectron spectrometer (Al-Kα non-monochromatic rays as the ray source). The C 1s binding energy of 284.6 eV is used as the calibration value. The element composition was analyzed using an Agilent 720 inductively coupled plasma atomic emission spectrometer (ICP AES) to determine the relative contents of ZCS-NiS_x. Ultraviolet-visible diffuse reflectance spectroscopy (DRS) was carried out with a LAMBDA 365 ultraviolet-visible spectrophotometer (PerkinElmer USA) with $BaSO_4$ as a reference. The nitrogen adsorption–desorption isotherm is measured on a Belsorp-max system to get the Brunauer–Emmett–Teller (BET) specific surface area and pore size distribution by Barrett–Joyner–Halenda (BJH) analysis. A fluorescence spectrometer (PerkinElmer USA) was used to characterize the photoluminescence (PL) spectrum and time-resolved fluorescence spectrum, and the maximum excitation wavelength was 420 nm. Electrochemical and photoelectrochemical measurements were measured in the three-electrode mode in 0.5 M Na_2SO_4 electrolyte solution on the CHI 660E electrochemical system. A Pt electrode and a saturated calomel electrode were employed as counter and reference electrodes, respectively. The test of linear sweep voltammograms and cyclic voltammogram (CV) curves was performed in 0.5 M H_2SO_4 aqueous solution, and linear sweep voltammetry (LSV) tests were conducted at a scan rate of 5 mV s^{-1}. In order to explore the charge features, the surface photovoltage (SPV) spectra were measured using self-made equipment.

Photocatalytic activity measurements

The photocatalytic H_2 evolution experiments were performed in a 300 mL quartz reactor under a 300 W xenon lamp (MICRO-SOLAR300, Perfectlight) with a 420 nm cutoff filter at ambient temperature. 10 mg of photocatalyst powder was ultrasonically dispersed in an aqueous solution (80 mL) of 10 vol% lactic acid (as a sacrificial agent). Before photocatalytic experiments, the reaction vessel was evacuated for 30 min to remove the dissolved oxygen. Next, the suspensions were stirred and irradiated under visible light. The hydrogen evolved was analyzed by gas chromatography (China; GC-9790 II, molecular sieve 5 A column, and N_2 carrier). The apparent quantum efficiency (AQE) for the H_2 evolution was measured using a similar experimental setup, with only a band-pass filter of 420 nm.

Results and discussion

The ultrafine ZCS nanoparticles modified with different contents of NiS_x were prepared by a facile photochemical deposition method. All samples were evaluated by XRD characterization to identify the crystalline structures and phase composition. As shown in Fig. 2a the reflections in the patterns of ZnS and CdS can be indexed to the cubic phase of zinc blende (JCPDS Card No. 05-0566) and the hexagonal phase of wurtzite CdS (JCPDS Card No. 65-2887), respectively. Significantly, the XRD diffraction peaks of ZCS can be assigned to both ZnS and CdS, which substantiates the successful formation of solid solution

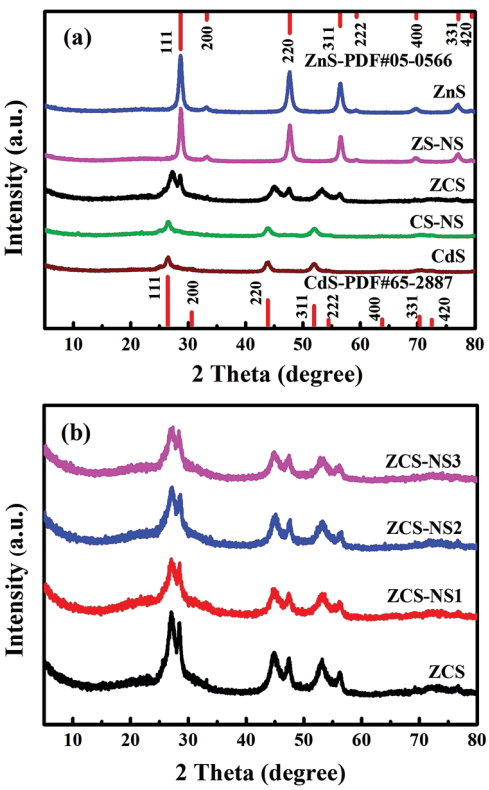

Fig. 2 The XRD patterns of (a) ZnS, CdS, ZCS, ZS-NS and CS-NS, (b) ZCS-NS1, ZCS-NS2, and ZCS-NS3.

structures with the coexistence of two different crystal phases. Compared with the corresponding pristine phase, the XRD patterns of ZS-NS, CS-NS and a series of NiS_x/ZnCdS showed no obvious difference on account of the low content and amorphous structures of NiS_x, as shown in Fig. 2a and b. What is more, no noticeable change could be detected with the nickel source concentration from 0.025 mmol to 0.1 mmol, further suggesting that NiS_x films coupled with ZCS nanoparticles have amorphous structures.

The characterization by SEM provided a general understanding about the morphology in Fig. S1 (ESI†). All samples exhibit the similar uniform ultrafine nanoparticles with a particle size of about 10 nm. TEM and HRTEM images reveal further details on the microstructure of ZCS-NS2. As shown in Fig. 3a and b, The TEM images show that the ZCS ultrafine nanoparticles are well supported on NiS_x films and a particle or cluster of particles is surrounded by a thin film. The EDX pattern (Fig. 3c) illustrates the obvious fluorescence signals corresponding to Cd, Zn, S and Ni. The HRTEM image clearly shows the lattice fringes, suggesting the well-defined crystal structure (Fig. 3b). The measured lattice spacing is about 0.317 nm, which can be assigned to the (111) crystal planes of ZnCdS. This agrees well with the XRD results. But it should also be noted that no clear lattice fringe is observed in the HRTEM image of the NiS_x film due to the amorphous structure. Scanning transmission electron microscopy (STEM) and corresponding energy dispersive spectroscopy (EDS) mapping show that Cd, Zn, S and Ni elements are homogeneously distributed in the ZCS-NS2 sample (Fig. 3d–h). The more accurate compositional information of the products was then evaluated with ICP-AES. The content of the Ni element is 2.47% in ZCS-NS2.

For further confirmation, sample ZCS-NSE with excess NiS_x was characterized. The signature diffraction peaks related to NiS_x did not show up even if the NiS_x amount increased significantly (Fig. S2, ESI†), indicating that the NiS_x film has an amorphous structure. This could also be verified by the TEM observations. As we expected, more obvious thin films could be found among the ZCS nanoparticles in Fig. 4a and b. Besides, no lattice fringe was observed in the HRTEM of the NiS_x film (Fig. 4b and c), indicating the amorphous feature of NiS_x, which can correspond with the results of XRD patterns. Fig. 4d–h exhibit the HAADF image of ZCS-NSE and its corresponding (EDS) mapping images, further indicating the characteristics of elemental distribution. Interestingly, the presence of both S and Ni elements in the areas of TEM image marked with white dotted lines could be confirmed, which is the corresponding location of the amorphous film. But Cd and Zn could not be found, which illustrates the formation of an amorphous film of NiS_x evidently.

The XPS analyses for ZCS-NS2, ZS-NS, and CS-NS were carried out to probe the surface chemical states of Ni and S elements. Fig. 5a shows the photoemission of the Ni 2p core level and the spectrum was further fitted carefully. The

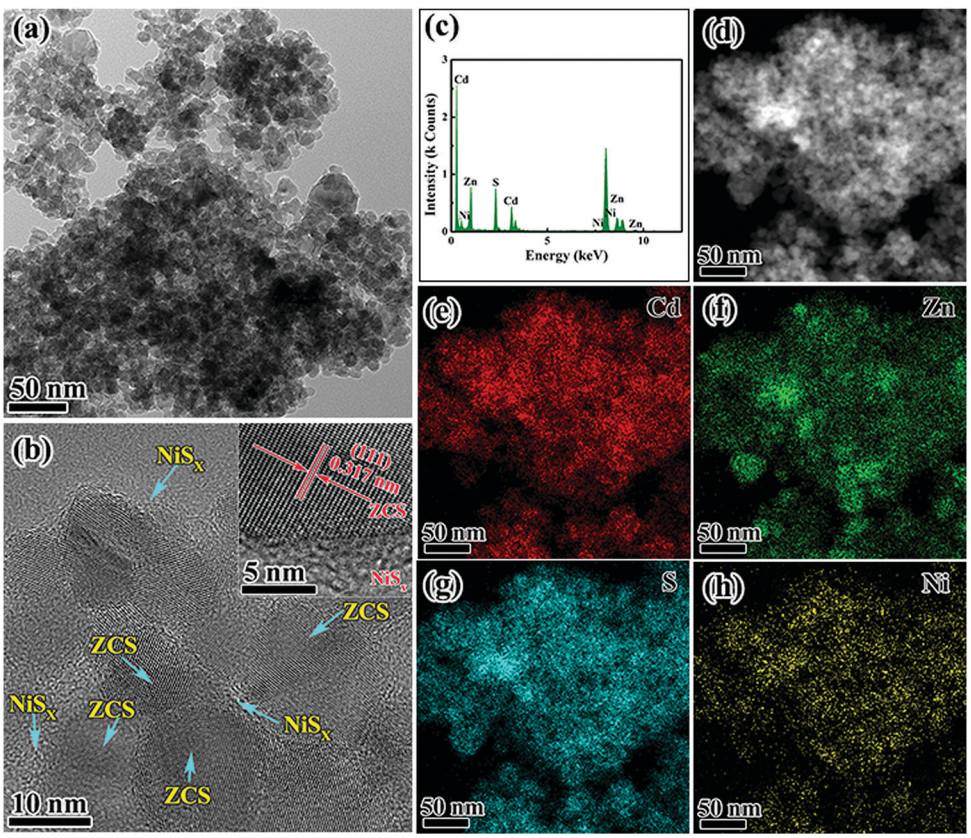

Fig. 3 TEM and HRTEM images (a and b), (c) EDX pattern, (d) STEM image, and the corresponding elemental mappings of (e) Cd, (f) Zn, (g) S, and (h) Ni elements of ZCS-NS2.

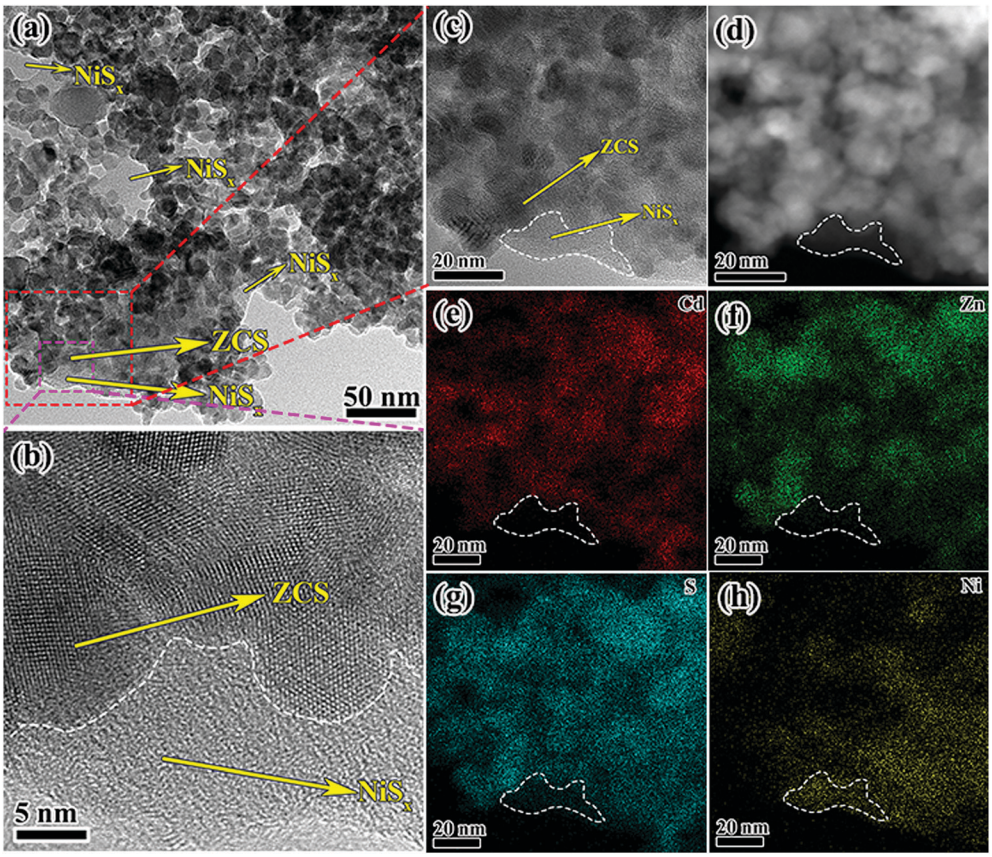

Fig. 4 TEM and HRTEM images (a and b), (c) EDX pattern, (d) STEM image, and the corresponding elemental mappings of (e) Cd, (f) Zn, (g) S, and (h) Ni elements of ZCS-NSE.

difference between the Ni $2p_{1/2}$ and Ni $2p_{3/2}$ peaks was assumed to be 17.4 eV according to the method.[22,35,40] The XPS peaks at 854.0.1 and 871.4 eV are assigned to Ni $2p_{3/2}$ and Ni $2p_{1/2}$, respectively, which is characteristic of Ni^{2+}. What cannot be ignored is that the peaks at 856.2 and 873.6 eV show higher binding energy, indicating the higher valence state of Ni species other than Ni^{2+}. This also implies that more than one type of Ni chemical state exists in the product. Two peaks at 861.8 and 879.4 eV are attributed to its satellite peaks. This is consistent with previous reports.[22,35] Similar conclusions can be drawn for the Ni in the ZS-NS and CS-NS (Fig. S3, ESI†). In the case of S, it can be deduced from the binding energy position that S is mainly present in a lower valence state. The high-resolution S spectrum of ZCS-NS2 indicated the existence of S $2p_{1/2}$ and S $2p_{2/3}$ peaks centered at 161.9 and 160.8 eV, respectively. In comparison with ZCS, the binding energies of S 2p in ZCS-NS2 shift towards low binding energy with 0.7 eV, which is attributed to the addition of NiS_x and the electronic interaction between ZCS and NiS_x. Therefore, the XPS results further confirm the existence of NiS_x and an intimate interfacial and electronic interaction between ZCS and NiS_x, which is in good agreement with the TEM results. This might benefit the photocatalytic performance of NiS_x/ZnCdS nanocomposites.

A larger specific area is conducive to more active sites for boosting the photocatalytic hydrogen generation. To understand the effect of the NiS_x film on the ZCS nanoparticle structure and specific surface area, N_2 adsorption–desorption isotherms of ZCS, ZCS-NS1, ZCS-NS2, and ZCS-NS3 and their corresponding pore-size distributions were investigated, as displayed in Fig. 6. According to Brunauer–Deming–Deming–Teller (BDDT) classification, N_2 adsorption/desorption isotherms of all samples are typical type IV isotherms, indicating the presence of a mesoporous structure. Pore-size distributions were calculated using the BJH method from the adsorption branch of the isotherms, and showed a relatively narrow range of 2–20 nm with a peak pore diameter of ~7 nm for all the samples. Table S1 (ESI†) shows the quantitative details of the S_{BET} and average pore sizes of the samples. The specific surface area of ZCS-NS2 is up to 96.30 $m^2\ g^{-1}$, which is slightly lower than that of ZCS due to the coverage of the NiS_x film on the surface to a certain extent. The high specific surface areas are possibly attributed to the ultrafine ZCS nanoparticles and the effectiveness of this synthetic method is proved. The results of N_2 adsorption–desorption measurement of the CdS, ZnS, CS-NS, and ZS-NS samples also support it, as shown in Fig. S4 and Table S1 (ESI†).

The light-harvesting properties of all samples were examined using diffuse reflectance UV-Vis spectroscopy, as shown in Fig. 7a. Compared with ZnS and CdS, it can be seen that there is a shift of the absorption edges in ZCS as a whole, showing that the prepared sample is not a simple mixture of ZnS and CdS, but

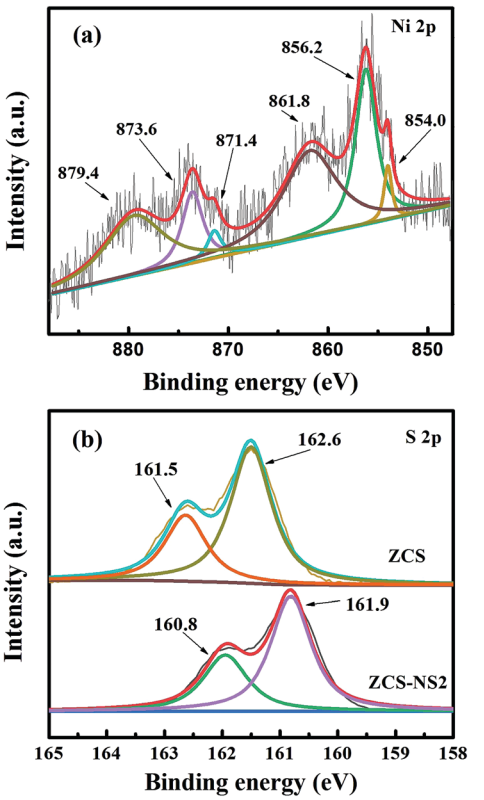

Fig. 5 High-resolution XPS spectra of (a) Ni 2p of ZCS-NS2 and (b) S 2p of ZCS-NS2 and ZCS.

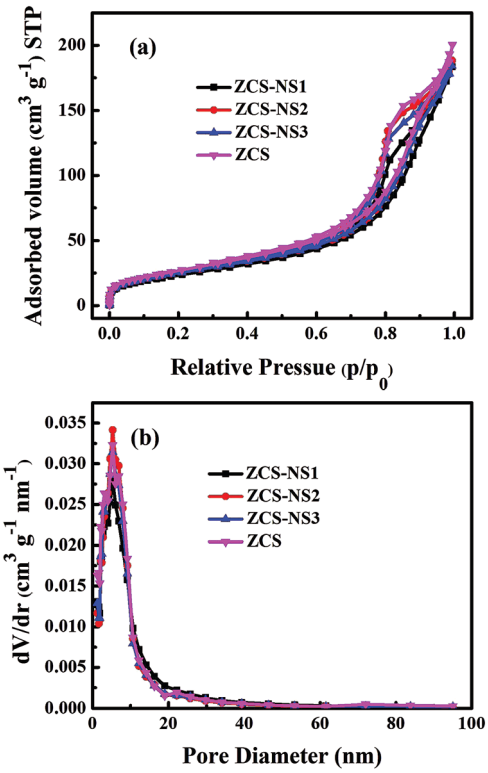

Fig. 6 Nitrogen adsorption/desorption isotherms and the corresponding pore-size distribution curves of the ZCS, ZCS-NS1, ZCS-NS2 and ZCS-NS3 samples.

ZnCdS solid solution. All of ZCS and NiS_x/ZnCdS possess absorption edges that extend into the visible region. With a gradual increase of NiS_x content, the intensities of visible-light spectra at wavelengths higher than 550 nm are much enhanced compared to that of the pristine ZCS. The curves of CS-NS and ZS-NS exhibit the same phenomenon. All suggest that growth of the NiS_x film promotes the harvest of the visible photons.

The significant improvements in the photochemical conversion efficiency of NiS_x/CdZnS composites were elucidated clearly under the visible-light photocatalytic H_2 production testing. As shown in Fig. 7b, the solid solution ZCS shows a relatively lower activity because of the rapid recombination of photogenerated electrons and holes, although it is better than that of the pristine CdS or ZnS. The introduction of the NiS_x film cocatalyst resulted in a significant enhancement in the photocatalytic H_2 production activity of NiS_x/ZnCdS. With increasing NiS_x content, ZCS-NS2 achieved an impressive value of 67.75 mmol g^{-1} h^{-1}, which showed 28.8-fold and 73.6-fold improvements for ZCS–Pt and pure ZCS in photocatalytic performance, respectively. Afterwards, the activity of ZCS-NS3 decreases because the high loading of the NiS_x film may shield the incident light which serves as a charge recombination center, implying that a suitable content of the NiS_x film cocatalyst is crucial for optimizing the H_2 production activities of composite photocatalysts. In comparison, Pt was photodeposited onto the ultrafine ZCS nanoparticles. The activity of ZCS–Pt is also shown in Fig. 7b, which is much lower than that of ZCS-NS2, indicating the NiS_x film as a potential alternative to the noble metal Pt. By extension, the much higher activities of CS-NS and ZS-NS than those of CdS and ZnS also clearly demonstrated the advantage of the amorphous NiS_x film cocatalyst (Fig. 7b). In order to understand the impact of the amorphous NiS_x film on the photocatalytic hydrogen production, the performances of many reported photocatalysts modified by nickel sulfide cocatalysts are listed for comparison (Table S2, ESI†). The superiority of the amorphous NiS_x film is thus clearly highlighted.

In order to determine AQE with wavelength dependence, the rates of H_2 evolution under the monochromatic light through 420, 500, and 520 nm band-pass filters were estimated under the same reaction conditions. As depicted in Fig. 7c, it is as expected that the rate of H_2 evolution and AQE of ZCS-NS2 increase dramatically compared with those of ZCS at different wavelengths. Table S3 (ESI†) shows the quantitative details of the rate of H_2 evolution and AQE of the samples. The trend of AQE closely followed that of absorbance behavior from UV-DRS. The AQE of the ZCS-NS2 composite is up to 10.24% at 420 nm. What is more, the stability of a photocatalyst is worth considering for its further practical application. Recycling H_2 evolution of ZCS-NS2 is shown in Fig. 7d. Only a slight loss of the H_2 evolution rate was observed after seven cycles, which is ascribed to the enrichment of photogenerated electrons on the amorphous NiS_x film so as to restrain the photocorrosion of ZCS. Thus the stability is greatly improved. Furthermore, the XRD analysis of ZCS-NS2

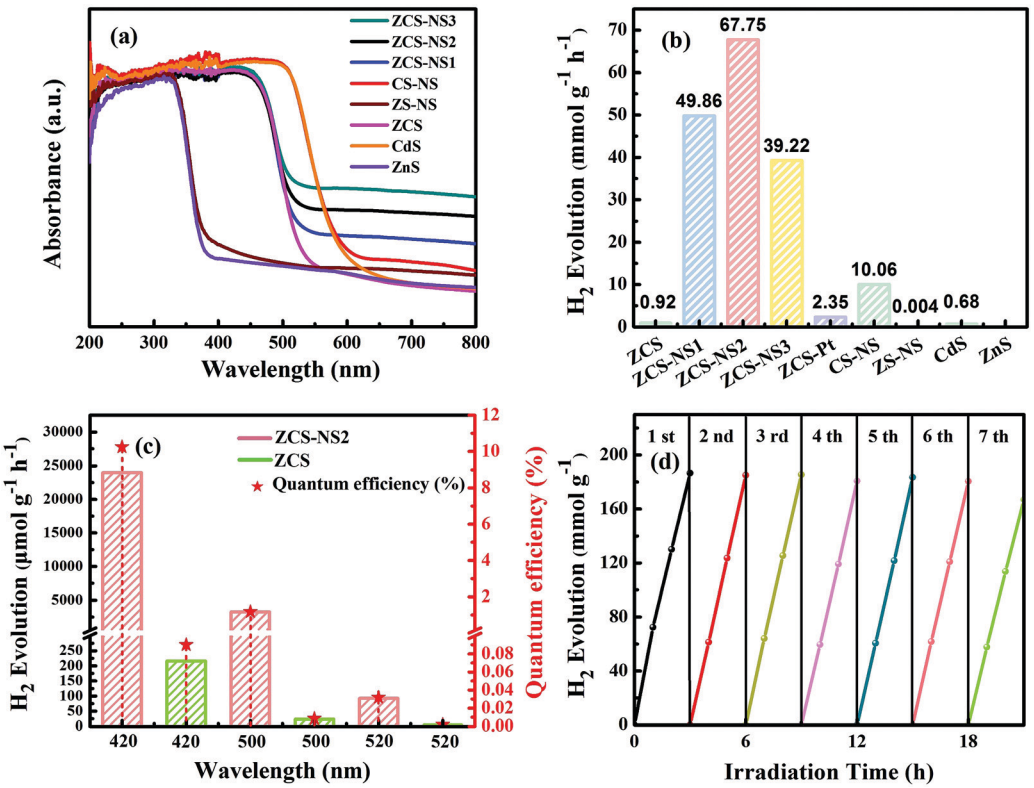

Fig. 7 (a) UV-Vis diffuse absorption spectra of the samples. (b) The comparison of photocatalytic H_2 production activities of different photocatalysts under visible light irradiation. (c) The photocatalytic hydrogen evolution rates under single-wavelength light and the corresponding AQE of ZCS and ZCS-ZS2. (d) Recycling H_2 evolution over ZCS-ZS2.

after seven cycles of photoreaction shows that no notable change can be found from the XRD patterns of the used catalyst (Fig. S5, ESI†), confirming its relatively good structural stability. Consequently, the relatively good photocatalytic performance and photostability might facilitate its potential applications in solar energy conversion.

The ZCS nanoparticles ingrained in the NiS_x films increased the efficient charge transport by the heterojunction interface and obviously decreased the recombination of electron–hole pairs evidenced by photoelectrochemical measurements. Fig. 8a shows the photocurrents *versus* time (*I*–*t*) curves of the samples for several on–off cycles of intermittent light irradiation. The photocurrent densities of all electrodes are repeatable and their photocurrents turn out to be in the order of ZCS-NS2 > CS-NS > ZCS-NS1 > ZCS-NS3 > ZCS > ZS-NS. The boosted photocurrent response of the ZCS-NS2 composites indicates a higher separation efficiency of the photoinduced electron–hole pairs and a lower recombination rate in such hybrid structures under visible-light illumination. Besides, EIS of the electrodes were measured to investigate the electrical conductivity (see Fig. 8b). ZCS-NS2 displays the smallest arc radius among all samples, indicating the smaller charge transfer resistance and suggesting that the electroconductivity was improved. It further confirmed the existence of strong coupling between ZCS ultrafine nanoparticles and NiS_x films and the enhanced electrical conductivity of ZCS-NS2 can be attributed to the synergistic effect between ZCS and NiS_x films. It is also worth noting that the content of NiS_x films greatly affects the electrochemical properties of the compositions.

The PL emission spectra also can be used to disclose the efficiency of charge carrier trapping and recombination of exited electrons and holes. A lower PL intensity might betoken a lower recombination rate of photo generated electrons and holes.[41] As shown in Fig. 8c, the PL spectrum of ZCS shows the strongest peaks among the samples. After the introduction of NiS_x films, the PL emission intensities of NiS_x/ZnCdS compositions decrease greatly, which indicated that electron–hole recombination can be better suppressed by the NiS_x cocatalyst. In particular, ZCS-NS2 was the most significant and it reveals the lowest emission peak intensity with respect to the other samples including CS-NS and ZS-NS photocatalysts, suggesting the highest separation efficiency of photoinduced charge carriers. This is ascribed to the fast interfacial electron transfer from ultrafine ZCS nanoparticles to NiS_x films at the optimized amount of NiS_x.[36] In a complementary measurement, we collected time-resolved PL decay curves. As can be seen in Fig. S6 (ESI†), the time-resolved PL decay curves of ZCS and ZCS-NS2 could be well fitted into a biexponential kinetics function and two components were derived. The decay parameters obtained from time-resolved fluorescence decay curves are summarized in Table S4 (ESI†). For the two components, the ZCS-NS2 composition yielded longer emission lifetime compared with ZCS. The observed extension of emission lifetime indicated that the charge recombination of ZCS-NS2 composition was inhibited, and thus the photoinduced electrons and holes could be more

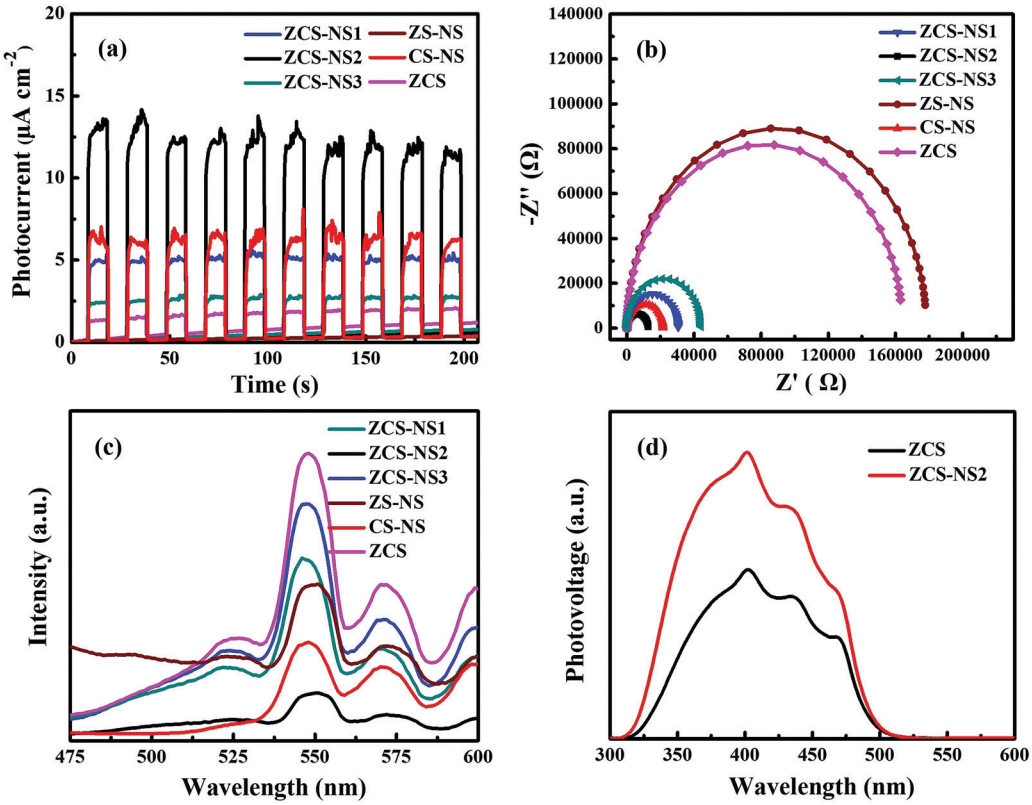

Fig. 8 (a) Transient photocurrent density curves, (b) electrochemical impedance spectra, and (c) photoluminescence spectra of various photocatalysts excited at 420 nm of ZCS-NS1, ZCS-NS2, ZCS-NS3, ZCS, CS-NS, and ZS-NS. (d) Steady-state SPV spectra of ZCS and ZCS-NS2.

effectively separated and taken advantage in the photocatalytic redox process.[42] This finding was further confirmed by SPV measurements. In general, some important factors are involved in the overall photocatalytic water splitting reaction, such as charge separation and migration to the surface of the semiconductor and surface reactions for H_2 or O_2 evolution. The steady-state SPV results (Fig. 8d) display the higher photovoltage on the surface of ZCS-NS2 than that on ZCS. In this case, it is acceptable that the strong SPV response corresponds to the high charge separation and the subsequent surface catalytic redox reactions.[42,43] This also supports that the coupling with the NiS_x film with massive reactive centers is expected to greatly accelerate its surface catalytic reactions and to be a promising and effective way to improve the photocatalytic performance in ZCS-NS2.

To further verify the advantages of the synergistic effect in ZCS-NS2, the Linear sweep voltammograms of the ZCS and ZCS-NS1, ZCS-NS2, and ZCS-NS3 electrodes were examined in 0.5 M H_2SO_4 aqueous electrolyte using a standard three-electrode system. The linear sweep voltammogram of the ZCS-NS2 heterojunctions shows a photocurrent density of 102 μA cm^{-2} at −1.4 V, which is larger than those of the ZCS (45 μA cm^{-2}), ZCS-NS1 (95 μA cm^{-2}) and ZCS-NS3 (64 μA cm^{-2}) in 0.5 M H_2SO_4 aqueous solution, as shown in Fig. 9a. So it displayed the best H_2 evolution activity of ZCS-NS2 compared to those of other samples, which also demonstrate that the heterostructure can optimize the interface electron structure to an enhanced intrinsic catalytic activity.[44,45] Moreover, the cyclic voltammetry (CV) tests of samples were conducted to determine the active surface area of samples. At a scan rate of 5 mV s^{-1}, ZCS-NS2 provides much higher current densities than those of ZCS, ZCS-NS1 and ZCS-NS3 (Fig. 9b), implying a much larger accessible electrochemical surface area and more exposed reactive sites of the ZCS-NS2 in low activation energy.[46] All of these results make it clear that the heterointerfaces of ZCS-NS2 accelerate the transfer of electrons and promote the reaction kinetics so as to facilitate the dissociation of H_2O molecules.

What is more, it is important to understand the route of the photon-generated electron transfer and diffusion, which depends on the band potential of the ZCS and the NiS_x co-catalyst. So the electrochemical Mott–Schottky plots of ZCS and ZCS-NS2 were obtained, as displayed in Fig. 10. Both of the positive slopes in the Mott–Schottky plots indicate that the samples are typical n-type semiconductors.[47] The flat band potentials of ZCS and ZCS-NS2 are estimated to be about −1.04 and −0.63 eV *versus* Ag/AgCl in Fig. 10a and b, respectively. Therefore, the Fermi level of ZCS and ZCS-NS2 could be calculated to be −0.84 and −0.43 eV according to the relationship of normal hydrogen electrode and AgCl (*vs.* 0.197 eV).[23,47] This leads to the conclusion that the photon-generated electron would transfer along the route of the ZCS to NiS_x, which benefits the separation and diffusion of the photon-generated carriers efficiently.

On the basis of the above characterization results and discussion, an illustration of possible interface electron

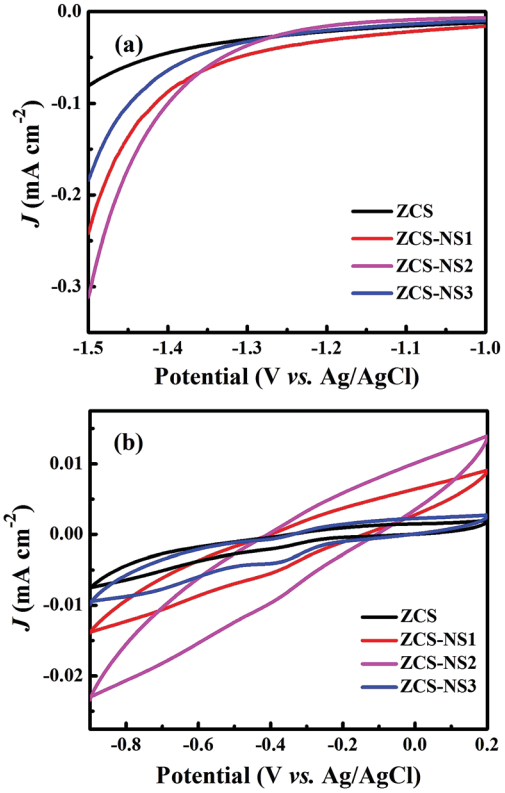

Fig. 9 (a) Linear sweep voltammograms of ZCS and NiS_x/ZnCdS in 0.5 M H_2SO_4 aqueous solution. (b) Typical cyclic voltammogram (CV) curves of ZCS and NiS_x/ZnCdS electrodes in 0.5 M H_2SO_4 aqueous solution with the scan rate of 5 mV s^{-1}.

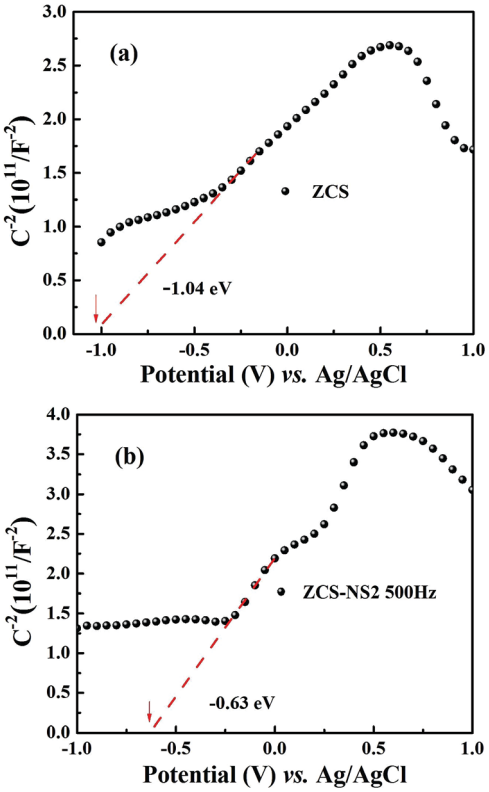

Fig. 10 The Mott–Schottky plots of ZCS and ZCS-NS2.

transfer behavior and the corresponding H_2-production mechanism is proposed in Fig. 11. Under visible light irradiation, the ultrafine ZCS nanoparticles absorb photons and can be easily excited and generate electrons and holes in the CB and VB, respectively. These photogenerated electrons and holes spread to the surface rapidly because the small size of the particles shortens the path of electron transfer and diminishes volume recombination. Normally, surface recombination is another thorny issue, resulting in a low photocatalytic activity of ZCS itself. However, in the NiS_x/ZnCdS system, due to the adequate contact and the more electron outlet points between ZCS nanoparticles and NiS_x films, the CB electrons of ZCS can be transported and dispersed on the surface of NiS_x effectively. Moreover, due to the characteristics of the electronic structure and amorphous film, NiS_x can function as an electron collector and conveyer prolonging the lifetime of the charge carriers,[48,49] during which the photogenerated electrons can efficiently migrate to reduce adsorbed H^+ ions and generate H_2 molecules. Meanwhile, the assembled holes on the VB of ZCS can be directly consumed by the sacrificial reagents (lactic acid) and then the photogenerated electrons can be further concentrated in the CB of ZCS.[50,51] Therefore, some of the advantages can elaborate the sharply enhanced photocatalytic H_2-production activity of NiS_x/ZnCdS compositions. First, ultrafine ZCS nanoparticles with large specific surface areas have good photo absorption efficiency reducing the transmission distance of photogenerated electrons. Secondly, introduction of NiS_x with good conductivity can facilitate the migration of photogenerated electrons from ZCS to separated active sites on NiS_x, thus greatly inhibiting their recombination and increasing the lifetime. Finally, the unique features of the amorphous NiS_x film can effectively collect the photogenerated electrons from the CB of ZCS, promote interfacial reaction kinetics facilitated charge transfer, and enlarge the reduction reaction space, which is responsible for the higher photocatalytic H_2 performance significantly.

Conclusions

In summary, we have successfully prepared a series of hybrid photocatalysts composed of ultrafine ZnCdS nanoparticles embedded in the amorphous NiS_x film by a simple photodeposition method. An extensive interface contact between the two semiconductors optimizes the path of photogenerated electron transfer, which produces more electron exit points of ZnCdS nanoparticles. In particular, the amorphous NiS_x films as cocatalysts could disperse electrons and expose abundant reducing active sites. Consequently, the NiS_x/ZnCdS hybrid photocatalyst boosts the H_2-generation performance and the highest photocatalytic H_2-generation rate reaches 67.75 mmol g^{-1} h^{-1} with an AQE value of 10.24% at 420 nm as well as exhibits excellent stability and repeatability. In this sense, it is believed that the efficient spatial transfer and separation of interfacial photoinduced carriers in the NiS_x/ZnCdS photocatalysts

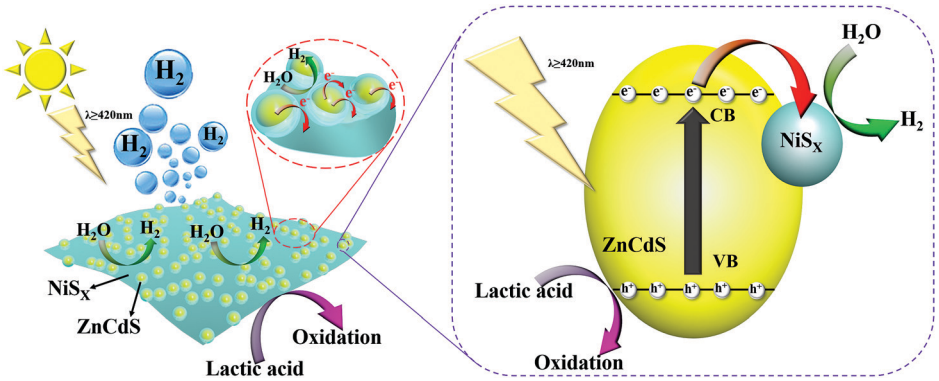

Fig. 11 Schematic illustration showing the possible mechanism involved in the process of photocatalytic H_2 production over NiS_x/ZnCdS photocatalysts under visible-light irradiation.

contribute to the remarkable photocatalytic activity. This work will help understand the electron–hole separation after the coupling of well-designed cocatalysts so as to explore excellent photocatalysts for cost-effective solar energy conversion.

Conflicts of interest

There are no conflicts to declare.

Acknowledgements

This work was financially supported by the NSF of China (No.: 21971143, 51572152 and 21805165), the 111 Project (D20015), and ITOYMR in the Higher Education Institutions of Hubei Province (T201904).

References

1 Q. Wang and K. Domen, *Chem. Rev.*, 2020, **120**, 919–985.
2 M. Z. Rahman, M. G. Kibria and C. B. Mullins, *Chem. Soc. Rev.*, 2020, **49**, 1887–1931.
3 Y. Bai, Z. Hu, J. X. Jiang and F. Huang, *Chem. – Asian J.*, 2020, **15**, 1780–1790.
4 Y. Wang, A. Vogel, M. Sachs, R. S. Sprick, L. Wilbraham, S. J. A. Moniz, R. Godin, M. A. Zwijnenburg, J. R. Durrant, A. I. Cooper and J. Tang, *Nat. Energy*, 2019, **4**, 746–760.
5 Z. Luo, T. Wang and J. Gong, *Chem. Soc. Rev.*, 2019, **48**, 2158–2181.
6 Z.-W. Zhang, Q.-H. Li, X.-Q. Qiao, D. Hou and D.-S. Li, *Chin. J. Catal.*, 2019, **40**, 371–379.
7 Z. Wang, C. Li and K. Domen, *Chem. Soc. Rev.*, 2019, **48**, 2109–2125.
8 H.-L. Wu, X.-B. Li, C.-H. Tung and L.-Z. Wu, *Adv. Mater.*, 2019, **31**, 1900709.
9 Y. Zhao, B. Zhao, J. Liu, G. Chen, R. Gao, S. Yao, M. Li, Q. Zhang, L. Gu, J. Xie, X. Wen, L. Z. Wu, C. H. Tung, D. Ma and T. Zhang, *Angew. Chem., Int. Ed.*, 2016, **55**, 4215–4219.
10 Y. Li, S. Wang, W. Chang, L. Zhang, Z. Wu, S. Song and Y. Xing, *J. Mater. Chem. A*, 2019, **7**, 20640–20648.
11 J. Ran, J. Zhang, J. Yu, M. Jaroniec and S. Z. Qiao, *Chem. Soc. Rev.*, 2014, **43**, 7787–7812.
12 J. Low, J. Yu, M. Jaroniec, S. Wageh and A. A. Al-Ghamdi, *Adv. Mater.*, 2017, **29**, 1601694.
13 X. B. Fan, S. Yu, H. L. Wu, Z. J. Li, Y. J. Gao, X. B. Li, L. P. Zhang, C. H. Tung and L. Z. Wu, *J. Mater. Chem. A*, 2018, **6**, 16328–16332.
14 S. Zhong, Y. Xi, S. Wu, Q. Liu, L. Zhao and S. Bai, *J. Mater. Chem. A*, 2020, **8**, 14863–14894.
15 X. Li, J. Yu, M. Jaroniec and X. Chen, *Chem. Rev.*, 2019, **119**, 3962–4179.
16 G. Li and Z. Tang, *Nanoscale*, 2014, **6**, 3995–4011.
17 S. Bai, L. Yang, C. Wang, Y. Lin, J. Lu, J. Jiang and Y. Xiong, *Angew. Chem., Int. Ed.*, 2015, **54**, 14810–14814.
18 X. Zhu, A. Yamamoto, S. Imai, A. Tanaka, H. Kominami and H. Yoshida, *Appl. Catal., B*, 2020, **274**, 119085.
19 X. Wang, C. Zhang, J. Du, X. Dong, S. Jian, L. Yan, Z. Gu and Y. Zhao, *ACS Nano*, 2019, **13**, 5947–5958.
20 H. Guan, S. Zhang, X. Cai, Q. Gao, X. Yu, X. Zhou, F. Peng, Y. Fang and S. Yang, *J. Mater. Chem. A*, 2019, **7**, 2560–2574.
21 F. Xue, M. Liu, C. Cheng, J. Deng and J. Shi, *ChemCatChem*, 2018, **10**, 5441–5448.
22 S. Meng, H. Wu, Y. Cui, X. Zheng, H. Wang, S. Chen, Y. Wang and X. Fu, *Appl. Catal., B*, 2020, **266**, 118617.
23 L. Jiang, K. Wang, X. Wu, G. Zhang and S. Yin, *ACS Appl. Mater. Interfaces*, 2019, **11**, 26898–26908.
24 C. Zhang, Y. Xu, C. Lv, L. Bai, J. Liao, Y. Zhai, H. Zhang and G. Chen, *Appl. Catal., B*, 2020, **264**, 118416.
25 W. Zhong, X. Wu, Y. Liu, X. Wang, J. Fan and H. Yu, *Appl. Catal., B*, 2021, **280**, 119455.
26 X.-Q. Wu, J. Zhao, Y.-P. Wu, W.-W. Dong, D.-S. Li, J.-R. Li and Q. Zhang, *ACS Appl. Mater. Interfaces*, 2018, **10**, 12740–12749.
27 J. Liu, Q. Jia, J. Long, X. Wang, Z. Gao and Q. Gu, *Appl. Catal., B*, 2018, **222**, 35–43.
28 Z. Peng, L. Jianping, T. Yonghua, C. Yuguang, L. Fei and G. Shaojun, *Appl. Catal., B*, 2018, **238**, 161–167.
29 Y. Zhang, Z. Peng, S. Guan and X. Fu, *Appl. Catal., B*, 2018, **224**, 1000–1008.

30 C. L. Bentley, C. Andronescu, M. Smialkowski, M. Kang, T. Tarnev, B. Marler, P. R. Unwin, U. P. Apfel and W. Schuhmann, *Angew. Chem., Int. Ed.*, 2018, **57**, 4093–4097.
31 X. Jia, Y. Zhao, G. Chen, L. Shang, R. Shi, X. Kang, G. I. N. Waterhouse, L.-Z. Wu, C.-H. Tung and T. Zhang, *Adv. Energy Mater.*, 2016, **6**, 1502585.
32 H. Fan, X. Huang, L. Shang, Y. Cao, Y. Zhao, L. Z. Wu, C. H. Tung, Y. Yin and T. Zhang, *Angew. Chem., Int. Ed.*, 2016, **55**, 2167–2170.
33 R. Shen, J. Xie, Q. Xiang, X. Chen, J. Jiang and X. Li, *Chin. J. Catal.*, 2019, **40**, 240–288.
34 J.-J. Wang, J. Wang, K. Feng, H.-H. Zhang, Z.-J. Li, B. Liu, C.-H. Tung and L.-Z. Wu, *J. Mater. Chem. A*, 2017, **5**, 9537–9543.
35 M. Liu, Y. Chen, J. Su, J. Shi, X. Wang and L. Guo, *Nat. Energy*, 2016, **1**, 16151.
36 C. Xue, H. Li, H. An, B. Yang, J. Wei and G. Yang, *ACS Catal.*, 2018, **8**, 1532–1545.
37 X. Zhao, J. Feng, J. Liu, W. Shi, G. Yang, G.-C. Wang and P. Cheng, *Angew. Chem., Int. Ed.*, 2018, **57**, 9790–9794.
38 F. Y. Tian, D. F. Hou, F. Tang, M. Deng, X. Q. Qiao, Q. C. Zhang, T. Wu and D. S. Li, *J. Mater. Chem. A*, 2018, **6**, 17086–17094.
39 C. Zhang, H. Liu, W. Wang, H. Qian, S. Cheng, Y. Wang, Z. Zha, Y. Zhong and Y. Hu, *Appl. Catal., B*, 2018, **239**, 309–316.
40 M. Lee, H.-S. Oh, M. K. Cho, J.-P. Ahn, Y. J. Hwang and B. K. Min, *Appl. Catal., B*, 2018, **233**, 130–135.
41 L. Jing, Y. Qu, B. Wang, S. Li, B. jiang, L. Yang, W. Fu, H. Fu and J. Sun, *Sol. Energy Mater. Sol. Cells*, 2006, **90**, 1773–1787.
42 B. Sun, W. Zhou, H. Li, L. Ren, P. Qiao, W. Li and H. Fu, *Adv. Mater.*, 2018, 1804282.
43 Q. Xu, H. Jiang, H. Zhang, Y. Hu and C. Li, *Appl. Catal., B*, 2019, **242**, 60–66.
44 Y. Zhang, J. Fu, H. Zhao, R. Jiang, F. Tian and R. Zhang, *Appl. Catal., B*, 2019, **257**, 117899.
45 Y.-P. Wu, W. Zhou, J. Zhao, W.-W. Dong, Y.-Q. Lan, D.-S. Li, C. Sun and X. Bu, *Angew. Chem., Int. Ed.*, 2017, **56**, 13001–13005.
46 G. Zhou, Y. Chen, H. Dong, L. Xu, X. Liu, C. Ge, D. Sun and Y. Tang, *Int. J. Hydrogen Energy*, 2019, **44**, 26338–26346.
47 J. Pan, B. Wang, Z. Dong, C. Zhao, Z. Jiang, C. Song, J. Wang, Y. Zheng and C. Li, *Int. J. Hydrogen Energy*, 2019, **44**, 19942–19952.
48 J. Zhang, L. Qi, J. Ran, J. Yu and S. Z. Qiao, *Adv. Energy Mater.*, 2014, **4**, 1301925.
49 Y. Yu and E. Wang, *Dalton Trans.*, 2018, **47**, 1171–1178.
50 M. Chen, P. Wu, Y. Zhu, S. Yang, Y. Lu and Z. Lin, *Int. J. Hydrogen Energy*, 2018, **43**, 10938–10949.
51 L. Li, J. Wu, B. Liu, X. Liu, C. Li, Y. Gong, Y. Huang and L. Pan, *Catal. Today*, 2018, **315**, 110–116.